Identification and modelling of the oxygen gas diffusion impedance in SOFC porous electrodes: application to Pr2NiO4+δ

Aurélien Flura, Clément Nicollet, Sébastien Fourcade, Vaibhav Vibhu, Aline Rougier, Jean-Marc. Bassat, Jean-Claude Grenier

Identification and modelling of the oxygen gas diffusion impedance in SOFC porous electrodes: application to $Pr_2NiO_{4+\delta}$

Flura Aurélien ; Nicollet Clément ; Fourcade Sébastien ; Vibhu Vaibhav ; Rougier Aline ; Bassat Jean-Marc, Grenier Jean-Claude
Affiliation : *CNRS, Université de Bordeaux, ICMCB, 87 Av. Dr Schweitzer, Pessac Cedex, F-33608, France*

Abstract

An in-depth analysis of the very low frequency impedance arcs observed when measuring efficient solid oxide fuel cell electrodes by electrochemical impedance spectroscopy (EIS) is reported in this paper. The study was carried out on $Pr_2NiO_{4+\delta}$//$Ce_{0.8}Gd_{0.2}O_{2-\delta}$//3 *mol.*% Y_2O_3-ZrO_2 symmetrical half-cell. In the temperature range 500–900 °C, three impedance arcs related to O_2 molecular diffusion were distinguished from the EIS measurements. Based on theoretical calculations using the Adler-Lane-Steele (ALS) and Dusty gas models, the arc at highest frequencies was ascribed to the diffusion of O_2 in the porous structures of the electrode and collecting gold grid. It obeys the ALS model, *i.e.* a parallel R//C impedance with a capacitance coming mainly from the solid phase. The second arc at medium frequencies was ascribed to the diffusion of O_2 in the porous structure of the ceramic part used to maintain the gold grid. It follows the Dusty gas model, *i.e.* a Warburg impedance with relaxation time depending on the gas phase properties. Finally, the third one at lowest frequencies was ascribed to the "gas conversion" phenomenon, coming from a difference in the local pO_2 above the active sites of the working and counter electrodes. This gas conversion impedance largely increases when clogging the channels of the gas distribution system.

Keywords : Gas diffusion impedance ; Adler-Lane-Steele model ; Dusty gas model ; Gas conversion impedance ; SOFC cathode

1. Introduction

One of the usual ways to characterize the intrinsic performances of the anode, electrolyte or cathode layers is to perform electrochemical impedance spectroscopy (EIS) measurements on symmetrical half cells [1]. In most cases, the EIS diagrams can be fitted and, on the basis of equivalent circuits, it is possible to separate the contributions from the various layers due to their difference in relaxation time. Typically, several more or less well-separated arcs are observed in the complex plane, representing for instance the ohmic loss in the electrolyte and the electrode reaction. In addition, various authors pointed out that low frequency arcs at $f < 100$ Hz are observable, and assigned them to transport limitations for supply of reactants and removal of products [2–6]. Such processes were named by Bessler [7] as "gas concentration impedance". Primdahl and Mogensen actually identified two arcs: the first one, at $f_{max} \approx 80$ Hz, was ascribed to gas diffusion limitations. The second one, at $f_{max} \approx 1$ Hz, was discussed in details and assigned to the so-called "gas conversion" [2,6]. This gas conversion impedance appears in particular when using a reference electrode exposed to a different atmosphere than the working electrode [2]. However, these authors reported that when the measurements were performed in a single gas atmosphere, gas conversion was not observed due to its very low polarization resistance value, and only the "gas diffusion impedance" was evidenced.

For SOFC cathodes, oxygen transport has been modelled by various authors [3,8,9]. For instance, Adler et al. [3] characterized a symmetrical $La_{0.6}Sr_{0.4}Fe_{0.8}Co_{0.2}O_{2-\delta}$//$Ce_{0.9}Gd_{0.1}O_{2-\delta}$ half-cell in air by EIS, and pointed out that oxygen transport in the porous structure of the electrode and/or in a stagnant layer above the electrode surface induces negligible polarization resistance values compared to the oxygen electrode reaction (OER). However, when performing EIS measurements at low pO_2, the authors showed that the gas diffusion impedance increases drastically, until it overlaps with the impedance related to the OER. Hence, it is of primary importance when performing EIS measurements at low pO_2 to minimize the impedance related to the O_2 diffusion in the setup. This is all the more essential since progress in the formulation of cathode materials has been made in the last decade. For instance, a polarization resistance as low as $R_p = 80$ mΩ·cm^2 was reported for a half-cell $Pr_2NiO_{4+\delta}$//$Ce_{0.8}Y_{0.2}O_{2-\delta}$//3 *mol.*% Y_2O_3-ZrO_2 at 600 °C in air [10].

* Corresponding author.
E-mail address: grenier@icmcb-bordeaux.cnrs.fr (J.-C. Grenier).

Nomenclature

c_v (mol/cm^3)	Bulk concentration of interstitial oxygen
C_i (F/cm^2)	Capacitance associated with process i
D_i (cm^2/s)	Diffusion coefficient for species i
d_{O2} (cm)	Diameter of the O_2 molecule
d_{pore} (cm)	Electrode pore diameter
F (C/mol)	Faraday constant
f_s (Hz)	Summit frequency of the impedance
f_{thermo} (dimensionless)	A thermodynamic factor
λ (cm)	Mean free path
l_{diff} (cm)	Molecular oxygen diffusion length
l_{elec} (cm)	Electrode thickness
m_i (g)	Weight for species i
M_i (g/mol)	Molar weight for species i
N_A (mol^{-1})	Avogadro number
P (atm)	Pressure
R (J/K/mol)	Gas constant
R_i (Ω·cm^2)	Area specific resistance associated with process i
ρ_i (g/mol)	Density for species i
ε (dimensionless)	Porosity
T (K or °C)	Temperature
T_i (s)	Relaxation time for process i
τ (dimensionless)	Tortuosity
V_i (cm^3)	Diffusion volume for species i
V_m (cm^3/mol)	Molar volume
w (s^{-1})	Frequency in radians
Z (Ω·cm^2)	Impedance

Recently, Yurkiv et al. [11] and Mortensen et al. [12] published extensive mathematical models for composite cathode/electrolyte SOFC electrodes. Using the appropriate software, a comprehensive simulation of the gas diffusion impedance, as well as of the OER at the electrode can be achieved.

The aim of this paper is to give a complete description of the oxygen diffusion occurring for a SOFC symmetrical half-cell, placed in an EIS measurement setup that has been optimized in terms of gas diffusion and current collecting at the electrodes. Praseodymium nickelate $Pr_2NiO_{4+\delta}$, further called PNO, was chosen as oxygen electrode due to its very low polarization resistance as reported in ref. [10], which allows better evidencing the gas diffusion impedance in the EIS diagrams. Using the Adler-Lane-Steele (ALS) [3] or the Dusty gas [13] models, the oxygen diffusion impedance contributions are calculated in the electrode porous structure and in the various parts of the setup. Then, the results of the EIS measurements and diagram fits are compared with the theoretical data and the various impedance contributions are identified.

In fine, one could use this study to reduce the gas diffusion impedance obtained in an EIS setup down to a minimum value.

2. Experimental

2.1. Preparation of cell components

Dense 3 *mol.*% Y_2O_3-ZrO_2 (*i.e.* TZ3Y from INDEC company) ceramic pellet of 90 μm thickness, Ø 25 mm diameter were used as electrolyte. Commercial sub-micronic powders were used as starting materials for preparing the barrier layer ($Ce_{0.8}Gd_{0.2}O_{1.90}$, GDC, Rhodia Comp.) and the porous cathodes, $Pr_2NiO_{4+\delta}$ (so called PNO) (Marion Technologies Comp.).

$Pr_2NiO_{4+\delta}$//GDC//TZ3Y symmetrical half-cells were prepared as follow: GDC interface layers were screen-printed on both sides of the electrolyte, and sintered at 1400 °C for 1 h, in air, with a controlled heating rate of 2 °C/min, resulting in ceria layer thickness of approximately 2 μm. Subsequently, $Pr_2NiO_{4+\delta}$ ink was screen-printed on top of the GDC interface layer and sintered at the optimized temperature [10] of 1150 °C, for 1 h, in air, with a heating rate of 2 °C/min. Cathode layers from 20 to 60 μm thickness were prepared by this method.

2.2. Electrochemical impedance spectroscopy measurements

The setup used to perform EIS measurement is depicted in Fig. 1.

The sample is maintained between two porous ceramic supports of 5 mm thickness, which are used to support the collecting gold grids (2 stacked gold grids on each side). A weight of around 335 g is applied on the upper porous ceramic plate, in order to obtain an efficient contact between the electrodes and the gold grids. This system was built-up to maximize the diffusion of O_2 in the setup.

Impedance measurements for the $Pr_2NiO_{4+\delta}$//GDC//TZ3Y symmetrical half-cells were carried out over the frequency range 10^6 Hz - 10^{-2} Hz, using an Autolab® PGStat 308 Frequency Response Analyser, the *ac* amplitude being fixed at 50 mV. Data were fitted using the Zview software (Scribner Associates®). The electrochemical experiments were performed from 500 °C up to 900 °C, in air, at i_{dc} = 0A. For specific characterizations, the oxygen partial pressure pO_2 was varied between 0.1 and 1 atm.

2.3. Scanning electron microscopy (SEM) observations

SEM images of half-cells cross-section were obtained using a Jeol JSM 6330F. Cells were embedded in epoxy resin (EpoFix from Struers A/S, Denmark) under vacuum, followed by a mirror polishing. Gold was subsequently sputtered on the resin top surface to avoid electrical charging. The thickness, porosity and pore diameter of the electrode were determined by means of image analysis using Image J opensource software.

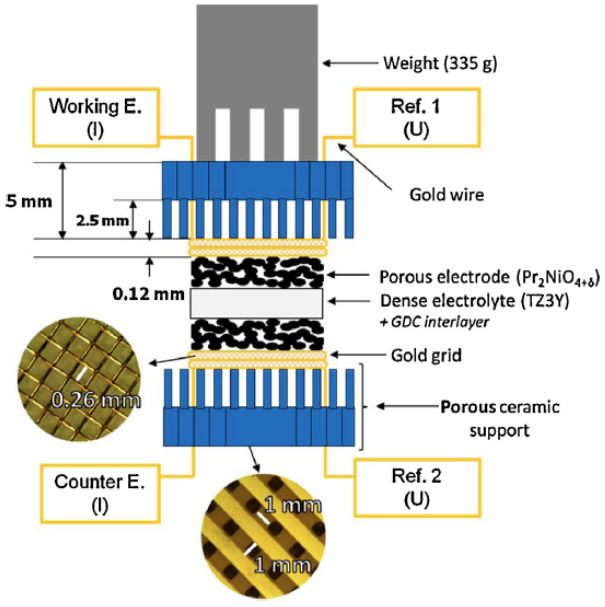

Fig. 1. Electrochemical impedance spectroscopy (EIS) measurement setup.

3. Results and Discussion

To model the O_2 molecular diffusion in the whole EIS setup - *i.e.* the porous ceramic and the gold grid - and in the $Pr_2NiO_{4+\delta}$ electrode, the determination of key parameters, as for instance the porosity and tortuosity of each part, is required.

3.1. Key geometric parameters determination

3.1.1. Geometric parameters of the $Pr_2NiO_{4+\delta}$ electrode

Key parameters as the porosity, tortuosity and pore diameter of the $Pr_2NiO_{4+\delta}$ electrode have been estimated from scanning electron microscopy (SEM) images of the polished cross-section of a standard $Pr_2NiO_{4+\delta}$//GDC//TZ3Y half cell. An example is shown in Fig. 2. One should point out that for PNO electrodes with thicknesses in the range 20 - 60 μm, used for the electrochemical impedance measurements, the microstructure does not change.

The porosity of the PNO electrode was determined from geometric consideration, based on the theoretical density of PNO at room temperature $\rho_{theo(PNO)} = 7.37\ g/cm^3$ and its geometric density. The PNO geometric density $\rho_{geo(PNO)}$ was determined from the parameters *i*) $m_{electrode}$ which is the weight of electrode deposited on TZ3Y, *ii*) $S_{electrode}$ which is the electrode surface, determined from a microscopy image of the electrode top surface using Image J software and *iii*) $l_{electrode}$ which is the average thickness of the electrode, determined from SEM micrographs. Finally, the geometric density can be determined *via* equation (13):

$$\rho_{geo(PNO)} = \frac{m_{electrode}}{S_{electrode} \times l_{electrode}} \quad (1)$$

The porosity is then calculated using equation (14):

$$\varepsilon = \frac{\rho_{theo(PNO)} - \rho_{geo(PNO)}}{\rho_{theo(PNO)}} \quad (2)$$

Geometrically, a porosity value $\varepsilon \approx 0.34$ was determined.

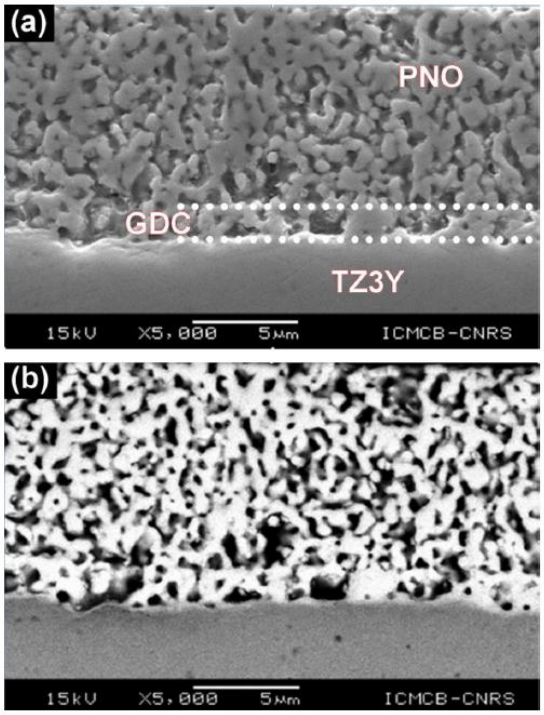

Fig. 2. SEM images of the polished cross-section of $Pr_2NiO_{4+\delta}$//GDC//TZ3Y (standard sample). (a) Secondary electrons (b) Backscattered electrons.

In addition, the porosity was cross-checked on backscattered electrons micrographs (*e.g.* Fig. 2b), by applying a threshold and calculating the black surface (corresponding to the pores) over the whole surface area ratio using Image J software. A value of $\varepsilon \approx 0.32$ was determined. Based on these two results, an average value of $\varepsilon \approx 0.33$ was used for the further calculations.

The average pore diameter of the porous PNO electrode was estimated from SEM micrographs (Fig. 2). Using Image J software, the pore diameter of PNO was measured on 10 micrographs. An average value $d_{pore} = 0.52$ μm was obtained.

The tortuosity τ reflects the extra distance, l', travelled by the gas through the porous structure of thickness l: $\tau = l'/l$. The studied electrode exhibits an open porosity with large channels; however, it is difficult to determine the value of the tortuosity. For this kind of microstructure, a value ranging from 1 to 3 is expected [14] . For the calculations, an average value $\tau = 1.5$ is further considered.

3.1.2. Geometric parameters of the EIS setup

Above the PNO top surface, diffusion of O_2 occurs in the EIS setup. Firstly, O_2 has to cross the collecting gold grid, which has the 1024 mesh/cm^2 specification, for a wire diameter of 0.06 mm, and a distance between two wires of 0.26 mm (Fig. 1). These parameters allows determining a porosity $\varepsilon \approx 0.66$ for a tortuosity $\tau = 1$. Two stacked gold grids being used for collecting the current, a thickness $l_{gold\ grid} = 0.12$ mm is considered.

Secondly, diffusion of O_2 occurs in the channel of the porous ceramic support. Channels are 1 mm wide (Fig. 1), separated by parallel 1 mm thick ceramic walls. A porosity $\varepsilon \approx 0.50$ for a tortuosity $\tau = 1$ can be estimated for this kind of architecture.

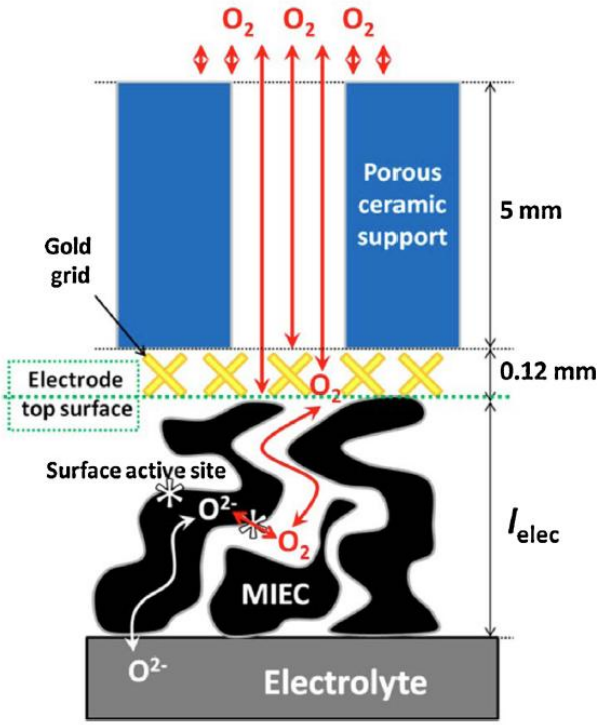

Fig. 3. O_2 diffusion pathway in the electrode and experimental EIS setup using a porous ceramic support.

3.2. Modelling of the O_2 molecular diffusion in the porous structure of $Pr_2NiO_{4+\delta}$ and the EIS setup

In a SOFC symmetrical cell, the exchange of O_2 between the gas phase and the electrolyte as shown in Fig. 3 can be described by the overall reaction [15,16]:

$$O_{2(g)} + 2V_O^{\bullet\bullet} + 4e^- \leftrightarrows 2O_{O(\text{electrolyte})}^X \quad (3)$$

$V_O^{\bullet\bullet}$ being an oxygen vacancy in Kröger-Vink notation, and $O_{O(\text{electrolyte})}^X$ an oxide ion in the electrolyte lattice.

Using this notation, for a mixed ionic electronic conducting (MIEC) lanthanide nickelate electrode, the overall reaction (3) can be decomposed into the following steps [3,8,11,17]

- Gas phase diffusion:

$$O_{2(g,\text{bulk})} \leftrightarrows O_{2(g,\text{electrode surface})} \quad (4)$$

$$O_{2(g,\text{electrode surface})} \leftrightarrows O_{2(g,\text{electrode active site})} \quad (5)$$

One can note that $O_{2(g,\text{bulk})}$ is related to the gas molecules located above the electrode top surface, starting from a point where the concentration in O_2 is constant. In between this point and the electrode active sites, a gradient in the O_2 concentration occurs due to the electrical potential.

- Adsorption – dissociation:

$$O_{2(g,\text{electrode active site})} + 2s \leftrightarrows 2O - s \quad (6)$$

with s being a surface active site.

- Oxygen chemical reduction:

$$O - s + Ni_{Ni}^X \leftrightarrows O^- - s + Ni_{Ni}^{\bullet} \quad (7)$$

$$O^- - s + Ni_{Ni}^X \leftrightarrows O''_{i(\text{MIEC,surface})} + Ni_{Ni}^{\bullet} + 1s \quad (8)$$

Reactions (7) and (8) can be also summarized as follows:

$$O - s + 2e^- \leftrightarrows O''_{i(\text{MIEC,surface})} \quad (9)$$

which characterizes the charge-transfer reaction at the electrode surface.

- Oxide ion diffusion in the MIEC oxide:

$$O''_{i(\text{MIEC,surface})} \leftrightarrows O''_{i(\text{MIEC,interface electrolyte})} \quad (10)$$

- Interfacial oxide ion transfer:

$$O''_{i(\text{MIEC,interface elect.})} + V_{O(\text{Electrolyte})}^{\bullet\bullet} \leftrightarrows O_{O(\text{Electrolyte})}^X \quad (11)$$

It should be mentioned that the oxygen diffusion path described above only takes into account the O^{2-} diffusion in the bulk of the MIEC; any oxygen species surface path diffusion is not considered [1].

This paper focuses on the reactions (4),(5) and (6), which are related to the diffusion of molecular O_2 species, and on the impedances related to these reactions.

Table 1
Effective diffusion coefficient D_{O_2,N_2}^{eff} expected from the O_2 diffusion in the porous structure of the $Pr_2NiO_{4+\delta}$ electrode ($d_{\text{pore}} = 0.52\,\mu m$, $\varepsilon = 0.33$, $\tau = 1.5$, $l_{\text{diff}} = 20\,\mu m$), together with the polarization resistances calculated with the ALS or Dusty gas models, and the capacitance calculated by the ALS model, from 600 °C up to 900 °C in air.

	Temperature (°C)			
	900	**800**	**700**	**600**
D_{O_2,N_2}^{eff} (cm^2/s)	0.20	0.18	0.17	0.15
$R_{\text{elec-ALS}}^{\text{gas diff}}$ ($m\Omega \cdot cm^2$)	0.48	0.44	0.40	0.37
$R_{\text{elec-DUSTY}}^{\text{gas diff}}$ ($m\Omega \cdot cm^2$)	0.24	0.22	0.20	0.18
$C_{\text{elec-ALS}}^{\text{gas diff}}$ (F/cm^2)	0.39	0.51	0.72	1.10

3.3. Gas diffusion impedance modelling

In a first stage, two models will be described: the ALS model that takes into account the contribution of the production/removal of oxygen at the surface active sites of the electrode (electrochemical source term) on the oxygen gas diffusion phenomenon, and the Dusty gas model that does not take into account this contribution.

3.3.1. The Adler-Lane-Steele (ALS) model

Within the ALS model that describes the oxygen electrode reaction in MIEC electrode, Adler et al. [3] considered the limiting case where the reaction would be controlled by gas phase diffusion in a stagnant film on top of the electrode surface. In that case, these authors modelled the impedance $Z_{\text{ALS}}^{\text{gas diff}}$ to obey the parallel R//C-like equation (3):

$$Z_{\text{ALS}}^{\text{gas diff}} = \frac{R_{\text{ALS}}^{\text{gas diff}}}{1 - jwR_{\text{ALS}}^{\text{gas diff}} \cdot C_{\text{ALS}}^{\text{gas diff}}} \quad (12)$$

with the polarization resistance $R_{\text{ALS}}^{\text{gas diff}}$ being directly dependent on the thickness of the gas boundary layer l_{bl} and on the effective diffusion coefficient of O_2, D_{O_2,N_2}^{eff} in air [1] given by equation (13):

$$R_{\text{ALS}}^{\text{gas diff}} = \frac{RT}{8F^2} \cdot \frac{l_{\text{bl}} \cdot V_m}{D_{O_2,N_2}^{\text{eff}}} \cdot \left(\frac{1 - p_{O_2}}{p_{O_2}}\right) \quad (13)$$

In equation (13), V_m represents the molar volume of the gas.

The capacitance $C_{\text{ALS}}^{\text{gas diff}}$ is given by equation (14):

$$C_{\text{ALS}}^{\text{gas diff}} = \frac{2F^2}{RT} \cdot \frac{(1-\varepsilon) l_{\text{elec}} \cdot c_v}{f_{\text{thermo}}} \quad (14)$$

with ε the porosity, c_v the vacancy concentration, l_{elec} the electrode thickness and f_{thermo} the thermodynamic factor of the MIEC electrode [18]. It should be pointed out that the capacitance comes primarily from the solid phase (electrode), since the atomic density of oxygen in the solid is much larger than in the gas phase.

Table 2
Effective diffusion coefficient expected from the O_2 diffusion in the porous structure of the $Pr_2NiO_{4+\delta}$ electrode ($d_{\text{pore}} = 0.52\,\mu m$, $\varepsilon = 0.33$, $\tau = 1.5$, $l_{\text{diff}} = 20\,\mu m$), together with the polarization resistances calculated with the ALS or Dusty gas model, and the capacitance predicted by the ALS model, at 900 °C, for various pO_2.

$T = 900$ °C	pO_2 (atm)			
	1	**air**	**0.01**	**0.001**
D_{O_2,N_2}^{eff} (cm^2/s)	0.20	0.20	0.20	0.20
$R_{\text{elec-ALS}}^{\text{gas diff}}$ ($m\Omega \cdot cm^2$)	≈ 0	0.48	12.6	128
$R_{\text{elec-DUSTY}}^{\text{gas diff}}$ ($m\Omega \cdot cm^2$)	≈ 0	0.24	6.32	64.0
$C_{\text{elec-ALS}}^{\text{gas diff}}$ (F/cm^2)	0.38	0.39	0.39	0.39

Table 3
Effective diffusion coefficient expected from the O_2 diffusion in the porous structure of the gold grid (d_{pore} = 0.26 mm, ε = 0.66, τ = 1, l_{diff} = 120 µm), together with the polarization resistances calculated with the ALS or Dusty gas models.

	Temperature (°C)			
	900	800	700	600
$D^{eff}_{O_2,N_2}$ (cm²/s)	1.50	1.28	1.08	0.90
$R^{gas\ diff}_{goldgrid-ALS}$ (mΩ·cm²)	0.39	0.38	0.37	0.36
$R^{gas\ diff}_{goldgrid-DUSTY}$ (mΩ·cm²)	0.19	0.19	0.19	0.18

3.3.2. The Dusty gas model

If the contribution of the electrochemical source term (*i.e.* the electrochemical production of O_2 related to the *ac* perturbation) to the oxygen diffusion is neglected, the Dusty gas model should be used for modelling purposes. In that case, a Warburg impedance should be observed experimentally [19], instead of a parallel R//C impedance as predicted by the ALS model.

If the diffusion of O_2 occurs over a finite distance l_{diff}, a finite-length Warburg (FLW) impedance $Z^{gas\ diff}_{FLW}$ is obtained according to equation (15):

$$Z^{gas\ diff}_{FLW} = R^{gas\ diff}_{FLW} \times \frac{\tanh\left(jwT^{gas\ diff}_{FLW}\right)^{p}}{\left(jwT^{gas\ diff}_{FLW}\right)^{p}} \quad (15)$$

Using the Dusty gas model [5,13,20], the theoretical gas diffusion polarization resistance $R^{gas\ diff}_{FLW}$ can be calculated using the equation (16):

$$R^{gas\ diff}_{FLW} = \frac{RT}{16F^2} \cdot \frac{l_{diff} \cdot V_m}{D^{eff}_{O_2,N_2}} \cdot \left(\frac{1-p_{O_2}}{p_{O_2}}\right) \quad (16)$$

The relaxation time $T^{gas\ diff}_{FLW}$ only depends on the effective gas phase diffusion of O_2 $D^{eff}_{O_2,N_2}$, and on the diffusion length.

$$T^{gas\ diff}_{FLW} = \frac{(l_{diff})^2}{D^{eff}_{O_2,N_2}} \quad (17)$$

It is interesting to note that a factor 2 separates the polarization resistance expected within the ALS model (equation (13)), from the R_p expected within the Dusty gas model (equation (16)).

In the following, the polarization resistance is calculated using the ALS model or the Dusty gas model in the three different parts of the EIS set up, *i.e.* the electrode, the gold grid and the ceramic support. For both models, it is first necessary to determine the effective diffusion coefficient of O_2, $D^{eff}_{O_2,N_2}$, in each part.

3.3.3. Diffusion of O_2 in the electrode

To determine the effective diffusion coefficient of O_2 in the porous PNO electrode, it is necessary to know whether the diffusion occurring in the electrode structure is of Knudsen type or not. It is the case when the pore size of the electrode is of the same order of magnitude than the mean free path λ of O_2 calculated using equation (18):

Table 4
Effective diffusion coefficient expected from the O_2 diffusion in the porous structure of the ceramic support (d_{pore} = 1 mm, ε = 0.50, τ = 1, l_{diff} = 5 mm), together with the polarization resistances calculated with the ALS or Dusty gas model.

	Temperature (°C)			
	900	800	700	600
$D^{eff}_{O_2,N_2}$ (cm²/s)	1.14	0.97	0.82	0.68
$R^{gas\ diff}_{ceramic-ALS}$ (mΩ·cm²)	21.4	21.0	20.4	19.9
$R^{gas\ diff}_{ceramic-DUSTY}$ (mΩ·cm²)	10.7	10.4	10.2	9.94

$$\lambda = \frac{RT}{\sqrt{2}PN_A\pi d^2_{O_2}} \times \frac{10}{1.01325} \quad (18)$$

where $d_{O_2} \approx 0.292$ nm is the diameter of the O_2 molecule, N_A is the Avogadro number and P the pressure. For instance, in the temperature range 600 °C - 900 °C, this relation leads to a value $\varepsilon \approx 0.35$- 0.41 µm. The size of the electrode pores estimated from the SEM micrographs (*cf.* Fig. 2) is $d_{pore} \approx 0.52$ µm. Both values are of the same order of magnitude. In that case, Bosanquet equation [21] is used to determine the oxygen diffusion coefficient $D^{Bos}_{O_2,N_2}$:

$$D^{Bos}_{O_2,N_2} = \left(\frac{1}{D^{Bulk}_{O_2,N_2}} + \frac{1}{D^{Knudsen}_{O_2,N_2}}\right)^{-1} \quad (19)$$

This equation reflects a mixed regime of diffusion, where the O_2 molecules collide with other O_2/N_2 molecules and/or with the pore walls. It is calculated from the bulk diffusion of O_2 in N_2 and the Knudsen diffusion. The Fuller empirical equation (20) is used to calculate the O_2 bulk diffusion as a function of temperature [22]:

$$D^{Bulk}_{O_2,N_2} = \frac{10^{-3} \times T^{1.75}}{P\left(V^{1/3}_{O_2} + V^{1/3}_{N_2}\right)^2} \times \left(\frac{1}{M_{O_2}} + \frac{1}{M_{N_2}}\right)^{1/2} \quad (20)$$

The diffusion volumes, V_{O_2} = 16.6 cm³ and V_{N_2} = 17.9 cm³, are taken from ref. [22].

The Knudsen diffusion [23,24] is calculated *via* equation (21):

$$D^{Knudsen}_{O_2,N_2} = \frac{1}{3} d_{pore} \left(\frac{8RT \times 10^7}{\pi M_{O_2}}\right)^{1/2} \quad (21)$$

with $d_{pore} \approx 0.52$ µm.

Then, $D^{eff}_{O_2,N_2}$ is obtained from $D^{Bos}_{O_2,N_2}$ corrected with the tortuosity and porosity of the electrode [25,26] :

$$D^{eff}_{O_2,N_2} = \frac{\varepsilon}{\tau} D^{Bos}_{O_2,N_2} \quad (22)$$

For the calculation, a porosity $\varepsilon \approx 0.33$ and tortuosity τ = 1.5 as determined in section 3.1.1, and an electrode thickness of 20 µm were considered.

The effective diffusion coefficient of O_2 in the porous electrode was determined in the temperature range 600 - 900 °C. The polarization resistances were then calculated from both models, together with the capacitances expected with the ALS model (Table 1).

To calculate the capacitance $C^{gas\ diff}_{elec-ALS}$ from the ALS model, values of the thermodynamic factor and of the vacancy concentration were determined from TGA experiments carried out at various pO_2 on PNO [27]: for instance, at 900 °C, $f_{thermo} \approx 3.3 \cdot 10^{-2}$ mol/cm³. More details for the calculation of the thermodynamic factor are given in Mauvy et al. [18].

These results show that for a pore diameter of 0.52 µm, a tortuosity τ = 1.5 and a porosity ε = 0.33, the effective diffusion coefficient of O_2, $D^{eff}_{O_2,N_2}$,in the porous structure of the electrode should not exceed a value as low as 0.20 cm²/s, at 900 °C. Given a diffusion length of 20 µm, the polarization resistance $R^{gas\ diff}_{elec?DUSTY}$, expected from pure diffusion should not exceed 0.24 mΩ·cm² at 900 °C, which is quite low. Twice the value is obtained when considering the chemical source term, as assumed by the ALS model.

In a second step, the influence of pO_2 was considered. Results of the calculation for a temperature of 900 °C are reported in Table 2.

It should be emphasized that the effective diffusion coefficient of O_2, $D^{eff}_{O_2,N_2}$, does not depend on pO_2. In addition, the capacitance predicted by the ALS model is stable at around 0.39 F/cm² over three decades of pO_2.

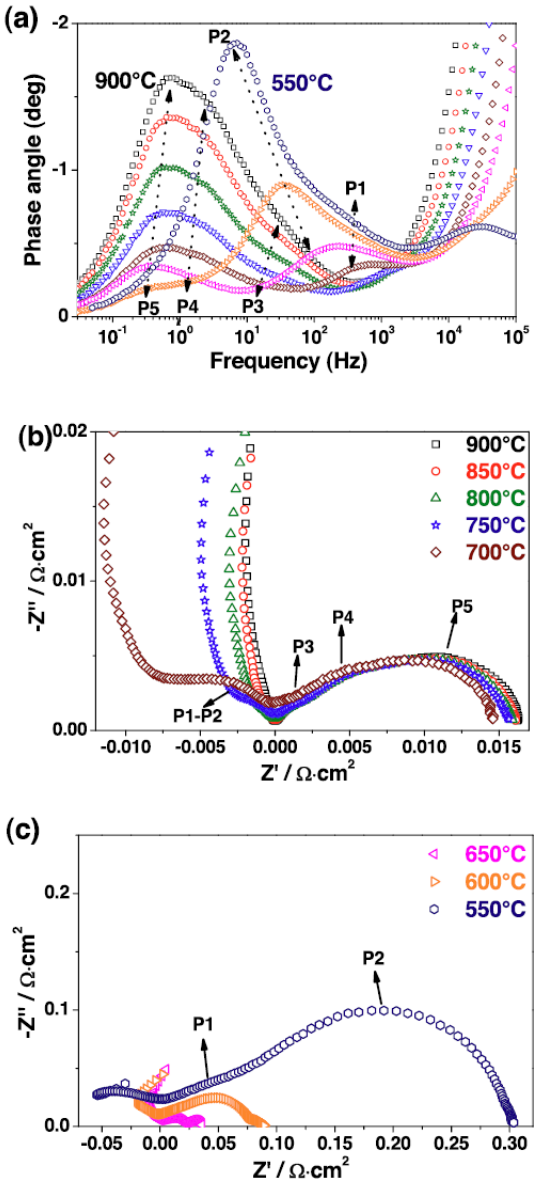

Fig. 4. EIS measurements of a $Pr_2NiO_{4+\delta}$(60 μm)//GDC//TZ3Y symmetrical half cell. (a) Bode plots. Nyquist plots: (b) from 900 °C down to 700 °C (c) from 650 °C down to 550 °C.

Table 5
Effective diffusion of O_2 $D^{eff}_{O_2,N_2}$ and diffusion length l_{diff} calculated from the polarization resistance $R^{gas\ diff}_{FLW}$ and relaxation time $T^{gas\ diff}_{FLW}$ of the Warburg impedances of the P3, P4 and P5 processes.

T = 900 °C	$R^{gas\ diff}_{FLW}$ mΩ·cm²	$T^{gas\ diff}_{FLW}$ s	$D^{eff}_{O_2,N_2}$ cm²/s	l_{diff} cm
P3	1.04	0.014	7.87	0.33
P4	5.6	0.14	2.56	0.59
P5	10.5	0.82	4.40	1.90

However, large polarization resistance values can be reached when pO_2 is decreased. For instance, $R^{gas\ diff}_{elec-DUSTY} = 64\ m\Omega\cdot cm^2$ may be observed for a single diffusion of O_2 in the electrode if pO_2 is decreased down to 10^{-3} atm.

Next step was the calculation of the polarization resistance related to the diffusion of O_2 through the gold grid.

3.3.4. Diffusion of O_2 in the gold grid

The same procedure as described above was applied to the diffusion of O_2 in the gold grid. The pore diameter of the gold grid being equal to 0.26 mm, which is much larger than the mean free path of O_2 whatever the temperature, no Knudsen diffusion should be taken into account. A porosity $\varepsilon = 0.66$, tortuosity $\tau = 1$ and $l_{diff} = 120\ \mu m$ was used for the calculations (*cf.* 3.1.2). The capacitance values are not reported in the Table 3: being mainly related to the PNO electrode parameters in the ALS model, they remain unchanged.

The effective diffusion coefficient of O_2 in the porous structure of the gold grid is quite high compared to those determined for the electrode, *e.g.* $D^{eff}_{O_2,N_2} = 1.50\ cm^2/s$ at 900 °C for the gold grid compared to $D^{eff}_{O_2,N_2} = 0.20\ cm^2/s$ for the electrode.

For a diffusion length of 120 μm, it leads to a polarization resistance $R^{gas\ diff}_{goldgrid?DUSTY} = 0.19\ m\Omega\cdot cm^2$ at 900 °C, which is in the same range than the one expected from the O_2 diffusion in the electrode.

Finally, oxygen diffusion in the ceramic support was considered.

3.3.5. Diffusion of O_2 through the ceramic support

Again, the Knudsen diffusion is not considered due to the large pores of the ceramic support ($d_{poreceramic} \approx 1$ mm). A porosity $\varepsilon \approx 0.50$ for a tortuosity $\tau = 1$ is used for the calculation, together with a diffusion length of 5 mm (*cf.* 3.1.2). Results are summarized in Table 4.

At 900 °C, the effective diffusion coefficient of O_2 in the porous structure of the ceramic support is estimated at $D^{eff}_{O_2,N_2} = 1.14\ cm^2/s$. If the diffusion occurs over the whole thickness of the ceramic support (*i.e.* 5 mm), quite large polarization resistance is expected, *e.g.* $R^{gas\ diff}_{ceramic-DUSTY} = 10.7\ m\Omega\cdot cm^2$ when considering pure diffusion.

Above the porous ceramic support, O_2 bulk diffusion will be observed, which the coefficient $D_{O_2,N_2} = 2.26\ cm^2/s$ at 900 °C as given by the Fuller equation (13).

From this first section, it can be concluded that in air, polarization resistances related to O_2 diffusion in the porous structure of the electrode or of the gold grid would be difficult to observe with regards to their low expected values, $R_p \approx 0.5\ m\Omega\cdot cm^2$. Conversely, the polarization resistance related to O_2 diffusion in the porous structure of the ceramic support will be observable if the diffusion occurs over a sufficiently long length.

3.3.6. Particular feature of EIS setup: the gas conversion impedance

When performing EIS measurements on symmetrical cell at very low frequencies, in the particular case where the O_2 partial pressure above the active sites of the working electrode is sufficiently different from the pO_2 above the active sites of the counter electrode, it is possible to observe the so-called "gas conversion impedance" [2] related to the Nernst potential of equation (23):

$$E = \frac{RT}{4F}\ln\left(\frac{p_{O_2,red}}{p_{O_2,ox}}\right) \quad (23)$$

Modelling shows that this gas conversion impedance obeys a parallel R//C like process, leading to an overpotential η, according to equation (24):

$$\eta = \frac{RT}{4F}\ln\left(\frac{p_{i,O_2} + \Delta p_{O_2}}{p_{i,O_2}}\right) \quad (24)$$

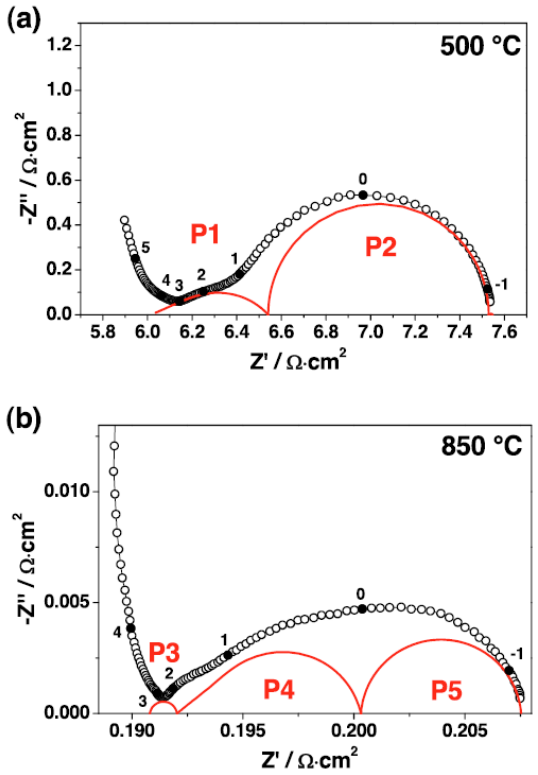

Fig. 5. Fit of the impedance diagrams of a $Pr_2NiO_{4+\delta}$//GDC//TZ3Y symmetrical half cell at (a) 500 °C and (b) 850 °C.

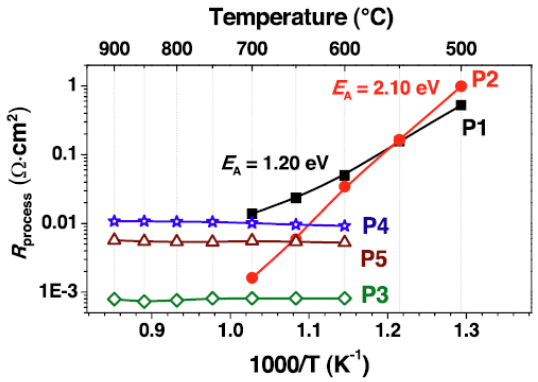

Fig. 6. Thermal variation of the polarization resistances of the different processes for a $Pr_2NiO_{4+\delta}$//GDC//TZ3Y half cell.

with p_{i,O_2} being the initial partial pressure in O_2 in a defined volume, and Δp_{O_2} the variation in pO_2 due to an *ac* perturbation.

Considering a constant *ac* perturbation, as used for EIS measurements, polarization resistances related to gas conversion impedances should decrease when the initial pO_2 or the volume of gas considered is increased. In addition, these authors showed that capacitances related to gas conversion impedances should increase with the volume of gas considered, alongside with the initial pO_2.

In the next section, EIS measurements were carried out on $Pr_2NiO_{4+\delta}$//GDC//TZ3Y half cells, in order to confront the experimental results with the theoretical calculations.

3.4. EIS measurements

EIS measurements were performed in air, from 500 °C up to 900 °C, on $Pr_2NiO_{4+\delta}$//GDC//TZ3Y half cells prepared as described in the experimental section.

For the current EIS experiments, 6 layers of PNO were screen-printed, leading to a total electrode thickness of 60 μm; in a next section, the influence of the thickness will be studied.

The Bode and Nyquist plots of the the impedance data are reported in Fig. 4; for the sake of clarity, the diagram at 500 °C is not shown. Below $f \approx 10^3$ Hz, all the diagrams fulfil the Kramers-Kronig relation.

Bode plots (Fig. 4a) allow distinguishing five processes, noted from P1 to P5, more or less visible in the temperature range from 900 °C down to 550 °C. It was necessary to consider these five processes in order to accurately fit the impedance diagrams. The processes P3, P4 and P5 that appear at low frequencies ($f < 100$ Hz, Fig. 4a), show very little thermal variation of R_p, and are gradually overlapped by the processes P1 and P2 at decreasing temperature (Fig. 4b&c).

These features clearly indicate that processes P3, P4 and P5 are related to molecular diffusion of O_2, while processes P1 and P2 are assigned to the oxygen electrode reaction in the solid phase [1]. This study is then focused on the processes P3, P4 and P5.

3.4.1. Fitting of the molecular O_2 diffusion impedances

In a first attempt, the contribution of the chemical source term to the oxygen diffusion was neglected, and the gas diffusion impedances were fitted considering the Dusty gas model, *i.e.* Warburg impedances. The effective diffusion coefficient of O_2, together with the diffusion length was determined in Table 5 for each process according to equations (16) and (17), for T = 900 °C.

The process P3 shows a $D^{eff}_{O_2,N_2} = 7.87\ cm^2/s$, which is much larger than the binary diffusion coefficient of O_2 in N_2 at 900 °C ($D^{bulk}_{O_2,N_2} = 2.27\ cm^2/s$, calculated from the Fuller equation (20)). P5 shows too large values of both $D^{eff}_{O_2,N_2} = 4.40\ cm^2/s$ and the diffusion length (at around 2 cm). It is then proposed that P3 and P5 cannot be assigned to the only diffusion of O_2 in a given medium: they should not be fitted with a Warburg element. Actually, they were successfully fitted with a parallel R//C impedance, as will be detailed below.

The process P4 shows a $D^{eff}_{O_2,N_2} = 2.56\ cm^2/s$, close to the binary diffusion of O_2 in N_2, with a diffusion length of 5.9 mm close to that of the ceramic support. It was well fitted with a Warburg impedance.

Results of the fits, using parallel R//C impedances for P3 and P5 and a Warburg impedance for P4, are shown in Fig. 5 at 500 °C and 850 °C.

In addition, at lower temperatures (*e.g.* $T = 500$ °C), better fits were obtained using a finite-length Warburg impedance for the P1 process and a R//CPE impedance for the P2 process. Indeed, P1 is likely to be related to O^{2-} solid state diffusion in an interphase formed at the interface PNO//GDC. P2 process is assigned to the oxygen electrode reaction at the PNO electrode: its R//C shape would be due to the relaxation of the oxygen exchange reaction at the interface gas//PNO. These points are however beyond the scope of the present study.

The values of the polarization resistance for the different processes are reported in Fig. 6.

As expected for gas diffusion impedances, the processes P3, P4 and P5 show almost no thermal activation. However, large activation energies are observed for the P1 and P2 processes, in agreement with oxygen electrode reaction phenomena.

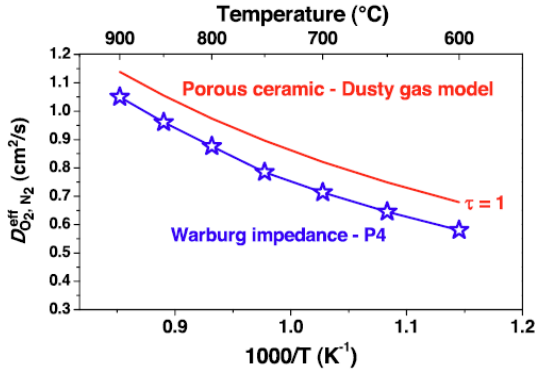

Fig. 7. Thermal variation of the effective O_2 diffusion, $D^{eff}_{O_2,N_2}$, extracted from the Warburg impedance of the P4 process. Comparison with the theoretical effective O_2 diffusion in the porous ceramic support calculated from the Dusty gas model.

Table 6
Influence of the temperature on the capacitances of the P3 and P5 processes.

	Capacitance (F/cm²)			
	900 °C	800 °C	700 °C	600 °C
P3	8.7	5.3	3.5	2.0
P5	64	78	82	107

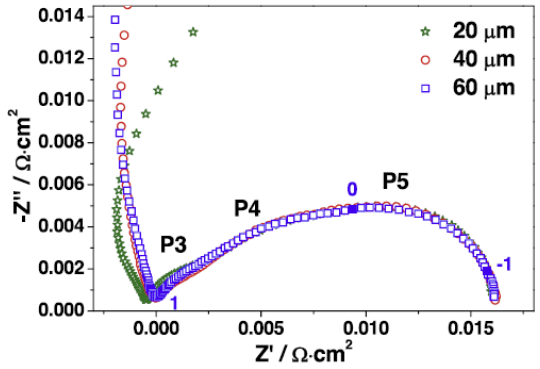

Fig. 8. Nyquist plots of the impedance diagrams of $Pr_2NiO_{4+\delta}$//GDC//TZ3Y half cells with different thicknesses of PNO (20, 40 or 60 µm), measured at 900 °C.

Table 7
Influence of the electrode thickness ($l_{elec.}$ = 20, 40 or 60 µm) on the P3 polarization resistance and capacitance.

P3	PNO electrode thickness l_{elec} (µm)		
	20	40	60
R_p(mΩ·cm²)	1.36	0.78	0.76
C(F/cm²)	2.73	4.34	8.7

From the finite-length Warburg used to fit P4, an effective diffusion coefficient of O_2 and a diffusion length was extracted over the temperature range 600–900 °C. The effective diffusion coefficient of O_2, $D^{eff}_{O_2,N_2}$, decreases linearly from 1.05 cm²/s at 900 °C, down to 0.58 cm²/s at 600 °C, while the diffusion length decreases from 4.6 mm at 900 °C down to 3.8 mm at 600 °C. A very good correlation was obtained between the effective diffusion coefficient of O_2 determined from the impedance data and those beforehand calculated for the porous ceramic support (Fig. 7).

The best correlation was obtained considering a tortuosity $\tau = 1.1$ in the porous ceramic support. It is interesting to note that the ceramic is composed of two parts (Fig. 1), with their respective channels perpendicular to each other. If the diffusion is straight in one part, when considering diffusion of O_2 through the two parts consecutively, the diffusion is not perfectly straight, and then the tortuosity should be larger than one.

From this study, it can be concluded that the process P4 is related to the O_2 diffusion in the ceramic support, following the Dusty gas model.

The capacitances obtained between 600 °C and 900 °C from the parallel R//C impedances of the processes P3 and P5 are reported in Table 6.

The experimental capacitance obtained for P3 (C_{P3} = 8.7 F/cm²) is within the range of the theoretical value calculated for a PNO electrode of 60 µm thick, at 900 °C, $C^{gas\ diff}_{elec-ALS}$ = 1.17 F/cm². However, the P3 capacitance value should theoretically increase at decreasing temperature, which is not in agreement with the experimental results.

The capacitance determined for P5 is quite large, C_{P5} = 64 F/cm² at 900 °C, and increases with decreasing temperature. Further studies were needed in order to identify these parameters. Firstly, the thickness of the PNO electrode was decreased from 60 µm down to 40 µm, and then down to 20 µm.

3.4.2. Influence of the electrode thickness

The Nyquist plot of the impedance diagrams measured at 900 °C on PNO//GDC//TZ3Y half cells with different thicknesses of PNO (20, 40 or 60 µm) are shown in Fig. 8.

The P4 and P5 processes were found to be invariant with the electrode thickness, which was expected for the process P4 related to the only diffusion of O_2 in the porous ceramic support. For the P5 process, it indicates that it does not primarily depend on the solid phase, which is quite interesting.

However, differences were observed for P3; they are reported in Table 7.

The value of the polarization resistance of P3 varies in the range 0.76–1.36 mΩ·cm², while the capacitance increases with the electrode thickness, which is consistent with equation (14) of the ALS model. If the evolution of the R_p does not follow the ALS model, the values R_p = 0.76–1.36 mΩ·cm² are in the range expected from the model, *e.g.* R_p = 0.87 mΩ·cm² for the diffusion of O_2 through 20 µm of PNO, then 120 µm of gold grid.

It is then proposed that P3 is related to diffusion of O_2 from the electrode active sites, into the porous structure of the electrode and of the gold grid, up to a distance around the edge of the ceramic support. The process is controlled by the formation/consumption of O_2 at the electrode active sites and the diffusion in the two media, and exhibits a capacitance related to the solid phase as predicted by the ALS model. Then at lower frequencies, P4 describes the diffusion of O_2 in the porous ceramic support, and is fitted using a Warburg element as proposed in the Dusty gas model. Parameters of the impedance are in that case dependent on the porous ceramic support geometry, not the electrode solid phase.

Finally, to assign P5, experiments at different partial oxygen pressures were carried out.

3.4.3. Influence of pO_2

The oxygen partial pressure was varied from pO_2 = 0.1 up to 0.45 atm, on a $Pr_2NiO_{4+\delta}$(60 µm)//GDC//TZ3Y half cell, at 900 °C. Nyquist plots of the impedance data are shown in Fig. 9.

In addition, the pO_2 dependence of the polarization resistance of each process was determined (Fig. 10).

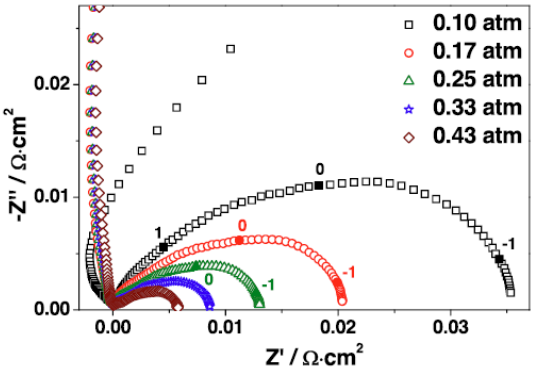

Fig. 9. Nyquist plots of the gas diffusion impedances for various pO_2 for $Pr_2NiO_{4+\delta}$/GDC//TZ3Y half cell.

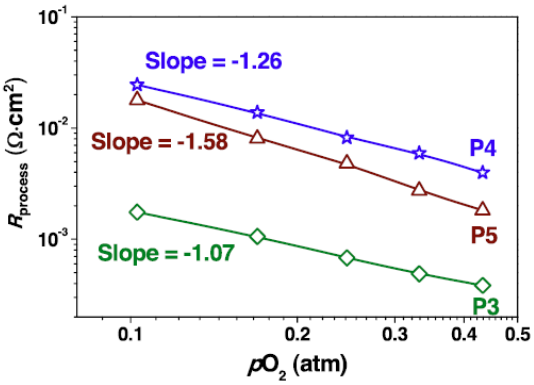

Fig. 10. Influence of the pO_2 on the polarization resistances of the gas diffusion impedances (processes P3, P4 and P5).

Table 8
Capacitance values of the P3 and P5 processes *vs.* pO_2.

pO_2 (atm)	Capacitance (F/cm²)				
	0.43	0.33	0.25	0.17	0.10
P3	4.1	5.4	6.3	8.1	10.2
P5	200	134	75.5	46.2	20.2

All the processes exhibit a pO_2 dependence larger or equal to 1, as expected for O_2 gas diffusion process. In agreement with the theoretical calculations, the effective diffusion coefficient of P4 was found to be invariant with pO_2 ($D^{eff}_{O_2,N_2} \approx 1.05\,cm^2/s$), as well as the diffusion length at around $l_{diff} = 4.6$ mm, which supports the previous conclusions.

The capacitances of P3 and P5 *vs.* pO_2 are reported in Table 8.

The capacitance of P3 decreases by approximately twice when pO_2 increases from 0.1 to 0.4 atm: it supports the conclusion that the process does not directly depends on the concentration of gaseous O_2 species, but rather on the concentration of O_2 in the electrode. It does however not completely agree with the theoretical calculation, since in this pO_2 range, the chemical capacitance of the solid phase should be more or less constant (*cf.* Table 2).

For P5, the capacitance of the process strongly increases with pO_2, by a factor ten. It clearly indicates that the process depends on the concentration of oxygen species in the gas phase. This point is developed in the next section.

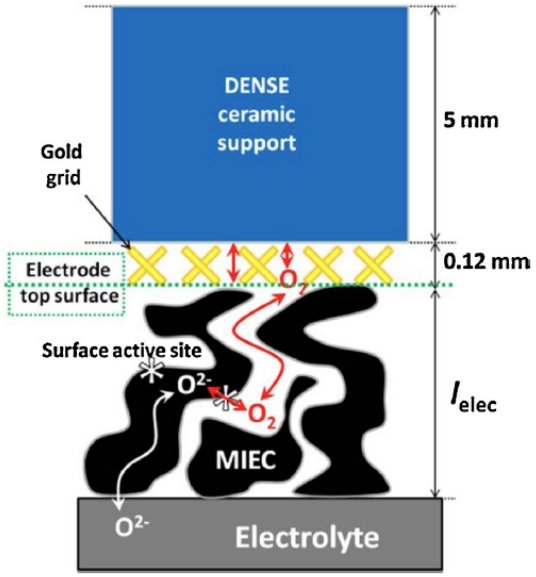

Fig. 11. Closed EIS setup.

3.4.4. Influence of the EIS setup

In this section, the porous ceramic support was replaced by a dense one, as shown in Fig. 11.

In that case, the volume of gas accessible for the active sites of the electrode is limited to the porous volume of the electrode and of the gold grid.

Impedance diagrams of a $Pr_2NiO_{4+\delta}$ (20 μm)//GDC//TZ3Y half cell recorded at 900 °C for different pO_2 is shown in Fig. 12.

With this closed setup, only one parallel R//C-like process was observed whatever the pO_2. The polarization resistance of the process was much larger than the total R_p of the gas diffusion processes obtained in the open setup. For instance, for $pO_2 \approx 0.4$ atm, $R_p \approx 52\,m\Omega\cdot cm^2$ was obtained in the closed setup, compared to $R_p \approx 6\,m\Omega\cdot cm^2$ when adding all the gas diffusion impedances in the open setup.

The polarization resistance of this process obtained at 900 °C, for different pO_2 is reported in Fig. 13.

R_p decreases when pO_2 increases, as expected for a gas diffusion process. Compared with Fig. 10, in the pO_2 range 0.1–0.5 atm, the slope of the process (1.23) is close to the slope of P5 (1.26).

The capacitance of this process *vs.* pO_2, reported in Table 9, increases with pO_2, as observed for P5 in Table 8.

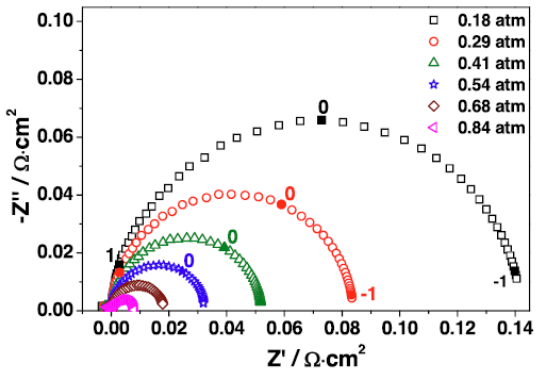

Fig. 12. Nyquist plot of the gas diffusion impedance *vs.* pO_2, at 900 °C for a $Pr_2NiO_{4+\delta}$(20 μm)//GDC//TZ3Y half cell, in a closed EIS setup.

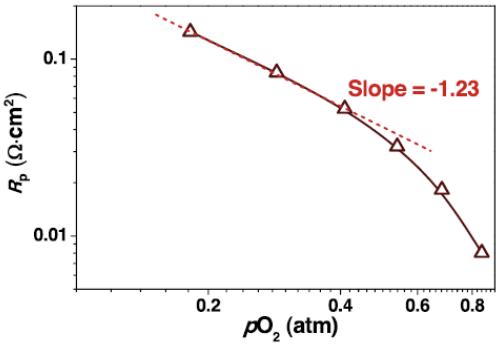

Fig. 13. Polarization resistance of the gas diffusion impedance *vs.* pO_2 in a closed EIS setup.

Table 9
Capacitance related to the gas diffusion impedance in a closed EIS setup *vs.* pO_2.

pO_2 (atm)	0.84	0.68	0.54	0.41	0.29	0.18
C (F/cm²)	10.4	4.7	2.6	1.7	1.2	1.1

However, the capacitance value is much lower: $C = 1.7$ F/cm^2 when $pO_2 \approx 0.4$ atm compared to $C \approx 200$ F/cm^2 for P5.

It is proposed that the process observed in the closed setup is the same than P5. The capacitance of this process is much lower in the closed setup due to the large decrease in the gas volume accessible to the electrode active sites, the latter being limited to the gas volume inside the porous structure of the electrode and of the collecting gold grids.

Given the overall characteristics of this process:

- a parallel R//C-like shape,
- a capacitance which increases with pO_2 and the gas volume accessible to the electrode active sites,
- a resistance which increases when pO_2 is decreased, and when the accessible gas volume is decreased,

it is proposed that P5 is a gas conversion process that appears when a significant difference in pO_2 exists above the electrode active sites of the working and counter electrode. This process becomes predominant compared to gas diffusion process (P3 and P4) when the gas volume above the electrode is restricted, or when the initial pO_2 is decreased. Indeed if the formation/consumption of O_2 generated by the EIS *ac* perturbation happens in a small gas volume, or in low pO_2 environment, the local difference in pO_2 between the working and counter electrode will be exacerbated, yielding significant increase of the polarization resistance. For instance $R_p = 141$ mΩ·cm^2 was observed at 900 °C for an initial $pO_2 = 0.18$ atm (Fig. 13). From the linear regression of the plot in Fig. 13, at $pO_2 = 1.10^{-2}$ atm, a polarization resistance $R_p \approx 7$ Ω·cm^2 could be extrapolated at 900 °C with this close setup.

To conclude, it clearly seems that for EIS setup with a poor gas diffusion network, this gas conversion impedance will appear during impedance measurements, and will become particularly problematic when carrying out low pO_2 experiments.

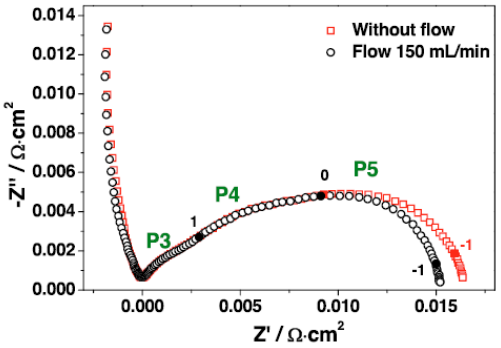

Fig. 14. Influence of the air flow on the gas diffusion impedances of a $Pr_2NiO_{4+\delta}$(60 μm)//GDC//TZ3Y half cell at 900 °C.

3.4.5. *Influence of the air flow*

In this section, using again the designed ceramic, the influence of a 150 mL/min air flow on the EIS measurements of the $Pr_2NiO_{4+\delta}$(60 μm)//GDC//TZ3Y half cell was studied at 900 °C; results are reported in Fig. 14.

In that case, it was found that the processes P3 and P4 were invariant with the air flow, which is not surprising since they are driven by the formation/consumption of O_2 at the electrode active sites, and their polarization resistance depends on the effective diffusion coefficient of O_2 in the porous structure of the electrode, gold grids and ceramic support.

Under air flow, the polarization resistance R_p of P5 decreased slightly, from 8.4 mΩ·cm^2 down to 6.5 mΩ·cm^2 and its capacitance did not change, in agreement with the previous conclusions. As the polarization resistance of the gas conversion process depends on the difference of pO_2 above the electrode active sites of the working and counter electrodes, which is driven by the *ac* voltage, applying a gas flow in the setup will reduce this local pO_2 difference. It could be expected from the gas flow to totally remove P5; it would imply that the gas can reach the electrode active sites. However, as shown by Aravind *et* al. [6] with a similar EIS setup, the gas will preferentially flow around the sample and EIS sample holder displayed in Fig. 1, rather than flow through the porous structures of the ceramic support, gold grids and electrode. A very specific EIS setup would be needed to clarify this point.

4. Conclusion

The O_2 diffusion phenomena occurring in SOFC symmetrical half-cell placed in an EIS measurement setup have been studied in 3 different parts, namely *i*) the electrode porous structure *ii*) the collecting gold grid and *iii*) the porous ceramic support used to maintain the collecting grid. The praseodymium nickelate $Pr_2NiO_{4+\delta}$ was chosen as the electrode material since it exhibits a very low polarization resistance, and allows focusing on the O_2 gas diffusion impedance. Modelling of the gas diffusion in the different parts of the setup was carried out using two models, the Adler-Lane-Steele model and the Dusty gas model. Conclusions of this theoretical approach showed that the polarization resistances related to the oxygen diffusion in the electrode or the gold grid will be rather low, while the R_p related to the diffusion in the porous ceramic support may be significant depending on its diffusion length.

It was experimentally shown that three processes related to diffusion of O_2 occur: the first one (at highest frequencies), a parallel R//C impedance in Nyquist representation, with $R_p \approx 0.8$ mΩ·cm^2 in air, comes from the O_2 diffusion in the porous structure of the electrode and of the gold grid, and exhibits a capacitance related to the solid phase as predicted by the ALS model. The second one (at medium frequencies), a finite-length Warburg impedance, with $R_p \approx 11$ mΩ·cm^2 in air, comes from the O_2 diffusion in the porous ceramic support above the collecting gold grids. In that case, the impedance is governed by parameters related to the ceramic support geometry, as for instance its effective diffusion coefficient of O_2.

The third process, a parallel R//C impedance at lowest frequencies, with $R_p \approx 6\ m\Omega \cdot cm^2$ in air was assigned to the so-called "gas conversion" phenomenon, which is related to a difference in the local pO_2 above the electrode active sites of the working and counter electrode in the EIS setup. This difference in pO_2 comes from the formation/consumption of O_2 at the electrode active sites, due to the EIS *ac* perturbation.

Using a closed EIS setup, *i.e.* a dense ceramic support, the polarization resistance associated with the gas conversion process largely increased, up to $R_p \approx 120\ m\Omega \cdot cm^2$ in air. It was correlated to the decrease of the gas volume accessible to the electrode active sites. In that case, only the gas conversion impedance could be observed, since it overlapped the gas diffusion processes namely in the electrode, collecting gold grid and porous ceramic support.

For an EIS setup with a poor gas distribution network, this gas conversion impedance will be very likely to appear and to become particularly large at low pO_2. This point is of importance when studying at low pO_2 the oxygen electrode reaction (OER) of any efficient electrode. Indeed, undesirable overlapping of the OER by this gas conversion impedance will be likely to occur in these conditions.

Acknowledgments

The research leading to these results has received funding from the European Union's Seventh Framework Programme (FP7/2007-2013) for Fuel Cells and Hydrogen Joint Technology Initiative under grant agreement n° [256768]. The authors gratefully acknowledge the European Community for supporting this work through the RAMSES project.

References

[1] S.B. Adler, Factors governing oxygen reduction in solid oxide fuel cell cathodes, Chem. Rev. 104 (2004) 4791–4843.
[2] S. Primdahl, M. Mogensen, Gas conversion impedance: a test geometry effect in characterization of solid oxide fuel cell anodes, J. Electrochem. Soc. 145 (1998) 2431–2438.
[3] S.B. Adler, J.A. Lane, B.C.H. Steele, Electrode kinetics of porous mixed-conducting oxygen electrodes, J. Electrochem. Soc. 143 (1996) 3554–3564.
[4] T. Jacobsen, P.V. Hendriksen, S. Koch, Diffusion and conversion impedance in solid oxide fuel cells, Electrochim. Acta 53 (2008) 7500–7508.
[5] A. Leonide, V. Sonn, A. Weber, E. Ivers-Tiffée, Evaluation and modeling of the cell resistance in anode-supported solid oxide fuel cells, J. Electrochem. Soc. 155 (2008) 36-41.
[6] P.V. Aravind, J.P. Ouweltjes, J. Schoonman, Diffusion impedance on nickel/gadolinia-doped ceria anodes for solid oxide fuel cells, J. Electrochem. Soc. 156 (2009) 1417- 1422.
[7] W.G. Bessler, Gas concentration impedance of solid oxide fuel cell anodes: I. Stagnation point flow geometry, J. Electrochem. Soc. 153 (2006) 1492–1504.
[8] J. Fleig, On the current-voltage characteristics of charge transfer reactions at mixed conducting electrodes on solid electrolytes, Phys. Chem. Chem. Phys. 7 (2005) 2027–2037.
[9] J. Nielsen, T. Jacobsen, M. Wandel, Impedance of porous IT-SOFC LSCF:CGO composite cathodes, Electrochim. Acta 56 (2011) 7963–7974.
[10] C. Ferchaud, J.C. Grenier, Y. Zhang-Steenwinkel, M.M.A. van Tuel, F.P.F. van Berkel, J.M. Bassat, High performance praseodymium nickelate oxide cathode for low temperature solid oxide fuel cell, J. Power Sources 196 (2011) 1872–1879.
[11] V. Yurkiv, R. Costa, Z. Ilhan, A. Ansar, W.G. Bessler, Impedance of the surface double layer of LSCF/CGO composite cathodes: an elementary kinetic model, J. Electrochem. Soc 161 (2014) F480–F492.
[12] J.E. Mortensen, M. Søgaard, T. Jacobsen, Analytical, 1-dimensional impedance model of a composite solid oxide fuel cell cathode, J. Electrochem. Soc. 161 (2014) F161–F175.
[13] E.A. Mason, A.P. Malinauskas, Gas transport in porous media: the Dusty gas model, Elsevier, Amsterdam, 1983.
[14] J. Joos, M. Ender, T. Carraro, A. Weber, E. Ivers-Tiffée, Representative volume element size for accurate solid oxide fuel cell cathode reconstructions from focused ion beam tomography data, Electrochim. Acta 82 (2012) 268–276.
[15] D.Y. Wang, A.S. Nowick, Cathodic and anodic polarization phenomena at platinum-electrodes with doped CeO_2 as electrolyte. 1. Steady-state overpotential, J. Electrochem. Soc. 126 (1979) 1155–1165.
[16] B.L. Kuzin, M.A. Komarov, Adsorption of O_2 at Pt and kinetics of the oxygen reaction at a porous Pt electrode in contact with a solid oxide electrolyte, Solid State Ionics 39 (1990) 163–172.
[17] S.P. Yoon, S.W. Nam, S.-G. Kim, S.-A. Hong, S.-H. Hyun, Characteristics of cathodic polarization at Pt/YSZ interface without the effect of electrode microstructure, J. Power Sources 115 (2003) 27–34.
[18] F. Mauvy, J.M. Bassat, E. Boehm, P. Dordor, J.C. Grenier, J.P. Loup, Chemical oxygen diffusion coefficient measurement by conductivity relaxation - correlation between tracer diffusion coefficient and chemical diffusion coefficient, J. Eur. Ceram.Soc. 24 (2004) 1265–1269.
[19] S. Primdahl, M. Mogensen, Gas diffusion impedance in characterization of solid oxide fuel cell anodes, J. Electrochem. Soc. 146 (1999) 2827–2833.
[20] J.W. Kim, A.V. Virkar, K.Z. Fung, K. Mehta, S.C. Singhal, Polarization effects in intermediate temperature, anode-supported solid oxide fuel cells, J. Electrochem. Soc. 146 (1999) 69–78.
[21] C.H. Bosanquet, British TA Report BR-507, British TA Report BR-507, 1944.
[22] J.R. Welty, C.E. Wicks, R.E. Wilson, Fundamentals of momentum, heat and mass transfer, John Wiley & Sons, New York, 1984.
[23] R. Jackson, Transport in porous catalysts, Elsevier, Amsterdam, 1977.
[24] R.B. Bird, W.E. Stewart, E.N. Lighfood, Transport phenomena, John Wiley & Sons, New York, 2002.
[25] N. Wakao, J.M. Smith, Diffusion in catalyst pellets, Chem. Eng. Sci. 17 (1962) 825–834.
[26] C.N. Satterfield, Mass transfer in heterogeneous catalysis, M.I.T. Press, Cambridge, 1970.
[27] A. Flura, S. Dru, C. Nicollet, V. Vibhu, S. Fourcade, E. Lebraud, A. Rougier, J.-M. Bassat, J.-C. Grenier, J. Solid State Chem. 228 (2015) 189–198.